Atmospheric Environment 384 (2026) 122331

Contents lists available at ScienceDirect

Atmospheric Environment

journal homepage: www.elsevier.com/locate/atmosenv

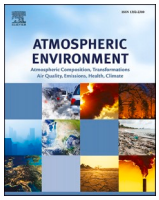

Study on the pollution characteristics of aerosols and VOCs along the lower reaches of the Yangtze River based on shipborne observations

Yixiang Chen [a,b], Ming Ding [c], Zhen Zhang [a,b,d,*], Saifen Yu [a,b,d], Qiuwei Xia [a,b,d], Daihao Yu [a,b], Jiawei Yang [a,b], Haiyun Xia [a,b,d]

[a] State Key Laboratory of Climate System Prediction and Risk Management (CPRM), NUIST, Nanjing, 210044, China
[b] School of Atmospheric Physics, Nanjing University of Information Science & Technology, Nanjing, 210044, China
[c] Jiangsu Provincial Environmental Monitoring Center, Nanjing, 210019, China
[d] Institute of Lidar Technology, GuangZai Co. Ltd., Hangzhou, 310005, China

HIGHLIGHTS

- First high spatiotemporal resolution shipborne observation of aerosols and VOCs following stricter fuel standards in the Yangtze River Delta
- Regional pollution transport has a significant impact on the pollution characteristics of local VOCs and aerosols.
- Shipborne polarization lidar captured three typical aerosol evolution episodes over the Yangtze River.
- VOCs exhibited distinct spatiotemporal heterogeneity, dominated by industrial halocarbons and port-related aromatics. Aromatics were critical precursors for regional SOA formation, with halocarbons showing negligible contributions.
- Shipping emissions and riverside industrial discharges jointly regulated riverine air pollution characteristics.

ARTICLE INFO

Keywords:
Shipborne measurement
Yangtze river delta
Linear depolarization ratio
Volatile organic compounds

ABSTRACT

China has faced complex air pollution challenges, particularly the synergistic evolution of particulate matter (PM) and its gaseous precursors. Although extensive near-ground observations exist, high-resolution insights into vertical distributions and chemical mechanisms along the Yangtze River via shipborne platforms remain limited. Shipborne measurements offer a unique advantage over fixed ground-based stations by enabling continuous spatial transects along the river, capturing spatial heterogeneity and vertical aerosol profiles that are inaccessible to point measurements alone. This study used a shipborne polarization lidar and single-photon ionization time-of-flight mass spectrometer to investigate spatiotemporal characteristics, sources, and evolution of aerosols and volatile organic compounds (VOCs) along the Yangtze River's Jiangsu section from 9 to 11 October 2022. Combined with ground data, we analyzed the temporal-spatial variations of vertical aerosol profiles, secondary organic aerosol (SOA) formation potentials (SOAP), and their interconnections. Three aerosol evolution episodes were identified: aged spherical particles via northwesterly regional transport; dust-mixed aerosols with high linear depolarization ratio (LDR) and low extinction coefficients; and aging of dust-polluted aerosols. VOCs showed strong spatiotemporal heterogeneity; high-pollution episodes were dominated by halogenated hydrocarbons and substituted aromatics, reflecting industrial emissions and solvent volatilization along the riverbanks. Xylene and ethylbenzene were linked to shipping and port activities. This represents the first high spatiotemporal resolution shipborne observation of aerosols and VOCs after the implementation of stricter fuel standards in the Yangtze River Delta, systematically revealing the VOC emission characteristics over the Yangtze River and the aging process of aerosols following regional transport.

* Corresponding author. State Key Laboratory of Climate System Prediction and Risk Management (CPRM), NUIST, Nanjing, 210044, China.
E-mail address: zhenzhang@nuist.edu.cn (Z. Zhang).

https://doi.org/10.1016/j.atmosenv.2026.122331
Received 2 June 2026; Received in revised form 3 August 2026; Accepted 26 August 2026
Available online 27 August 2026

1. Introduction

Air pollution in China has long been a pressing issue. More than a decade ago, the frequent occurrence of regional haze had already drawn widespread attention from both the public and the scientific community (Ming et al., 2017). As one of the most economically vibrant and highly urbanized regions in China, the Yangtze River Delta (YRD) region is characterized by intense emissions and complex pollutant profiles. It has consistently been a hotspot for complex air pollution, where fine particulate matter and ozone pollution alternate or co-occur, posing a severe threat to public health (Hamanaka and Mutlu, 2025).Historically, observational studies have predominantly focused on individual city clusters and relied on fixed ground-based stations, which effectively capture pollution characteristics at the urban scale(An et al., 2015; Wang et al., 2015, 2016, 2018). To clarify the spatial distribution and regional transport mechanisms of pollutants, prior studies have commonly adopted numerical methods including backward trajectories and chemical transport models to perform simulation and source apportionment. However, these models are inherently susceptible to uncertainties associated with emission inventories, meteorological fields, and chemical mechanisms.

Mobile monitoring of air quality has been extensively implemented worldwide. Early research primarily concentrated on the stationary and mobile sampling of PM and the six criteria air pollutants. In recent years, driven by the iterative advancement of high-precision observational instruments, online mobile monitoring technologies for volatile organic compounds including Time-of-Flight Mass Spectrometry (TOF-MS) and Gas Chromatography-Mass Spectrometry (GC-MS), as well as spectral remote sensing techniques such as Differential Optical Absorption Spectroscopy (DOAS) and Fourier Transform Infrared Spectroscopy (FTIR), have rapidly emerged (Huang et al., 2021; Tan et al., 2018; Wang et al., 2021). By integrating these techniques with vertical observation devices including polarization lidars and aerosol physicochemical analyzers, a multi-component mobile observation system is constructed, which effectively narrows the scale discrepancy between fixed-site monitoring and numerical model simulations.

In recent years, numerous studies have focused on air pollution along the middle and lower reaches of the Yangtze River, revealing significant differences between the atmospheric pollution over the river and that within the adjacent urban agglomerations. In the winter of 2015, institutions including Fudan University and the University of Science and Technology of China conducted a large-scale shipborne mobile observation campaign along the middle and lower reaches of the Yangtze River. The vessel departed from Shanghai on 21 November, arrived in Wuhan on 29 November, and returned to Shanghai on 4 December. A variety of observational instruments were deployed during this campaign, including analyzers for the physical and chemical properties of aerosols, monitors for six criteria air pollutants, VOCs sampling and monitoring devices, polarization lidars, and MAX-DOAS. This deployment enabled three-dimensional observations ranging from near-surface chemical compositions to vertical aerosol profiles(Fan et al., 2018; Hong et al., 2018; Li et al., 2018; Ting et al., 2021; Wang et al., 2020; Zhu et al., 2018). The campaign directly captured significant regional disparities in pollutant concentrations and sources. Specifically, it identified that Wuhan was dominated by secondary inorganic aerosols, the Yangtze River Delta was enriched in crustal elements, rural areas were prominently affected by biomass burning, and ship emissions contributed significantly in the Shanghai segment. Furthermore, observations from instruments like MAX-DOAS confirmed that severe pollution events in this basin were primarily driven by meteorologically induced cross-regional transport, rather than the accumulation of local emissions. Meanwhile, it pointed out that biomass burning was the dominant source of brown carbon light absorption in winter. Although the synchronous deployment of multiple instruments in this campaign yielded commendable data and results, the subsequent analyses predominantly focused on findings from individual instruments. Furthermore, the prolonged sampling times required for offline VOC and aerosol measurements limited the potential for high-temporal-resolution cross--validation and synergistic multi-pollutant source apportionment, leaving considerable room for optimization. Building upon the 2015 study, the Jiangsu Provincial Environmental Monitoring Center conducted a 15-day shipborne campaign along the Jiangsu segment of the Yangtze River in 2019, targeting the more heavily polluted lower reaches(Chen et al., 2022; Zhao et al., 2021). The study revealed that air pollution levels over the Yangtze River were higher than those in surrounding cities, with secondary nitrates, ship emissions, and coal combustion identified as the major sources of aerosols. The levels of the six criteria pollutants over the river were consistently higher than those at the nearest environmental monitoring stations, indicating a more profound impact from ship emissions in the riverine area and industrial discharges along the riverbanks.

Concurrently, from 2016 to 2020, increasingly stringent fuel standards were enforced across all navigable segments of the Yangtze River basin, mandating that ocean-going vessels switch to fuels with a sulfur content of $\leq$0.1% upon entering inland waterways. The Yangtze River Delta (YRD) region features a highly developed shipping industry. Estimations based on ship trajectories reveal that ship emissions exert a significant impact on the atmospheric environment(Fan et al., 2016). Furthermore, ship emission inventories indicate that emissions peak during hoteling and cargo-handling operations, while those from slow steaming and cruising modes are also prominent (Weng et al., 2020). During the initial phase of the fuel switch, sulfate emissions decreased (Xiao et al., 2018); however, the emission factors of VOCs increased significantly. Alkenes replaced alkanes as the dominant species, leading to an approximately twofold increase in the secondary organic aerosol formation potential (SOAFP) (Wu et al., 2020). Following the complete implementation of the fuel switch, aromatics and oxygenated VOCs (OVOCs) became the predominant VOC components, accompanied by further elevated emission factors and a marked enhancement in SOAFP (Zhang et al., 2024) Beyond the shifts in the emission profiles of major pollution sources over the Yangtze River driven by the revised marine fuel standards, the landscape of pollution sources in the YRD has undergone new transformations. Over the past decade, propelled by rapid urbanization and stricter environmental quality controls, coupled with the logistical convenience and cost-effectiveness of Yangtze River shipping, a substantial number of polluting enterprises have relocated from urban centers to riverside industrial parks.

In summary, the composition, source structure, and spatial distribution of air pollution along the middle and lower reaches of the Yangtze River exhibit unique characteristics that are distinct from those in urban areas. Furthermore, previous studies suffered from insufficient spatiotemporal resolution for VOC measurements. Given that the dominant sources of VOC emissions have shifted in recent years, the absence of corresponding cross-regional joint monitoring campaigns highlights a critical need for further investigation.

To address these gaps, our team conducted a shipborne mobile observation campaign along the Jiangsu segment of the Yangtze River between 9 and 11 October, 2022, utilizing a polarization lidar and a single-photon ionization mass spectrometer. This study focuses on analyzing the vertical distribution and optical properties of aerosols, as well as the spatiotemporal patterns of VOC components over this waterway. The campaign revealed distinct differences in VOC distributions between port operation areas and riverside industrial zones, elucidating the characteristic profiles of VOC emissions from various sources. Concurrently, we successfully captured the aging process of dust aerosols and systematically analyzed the evolution of key parameters, such as the LDR and extinction coefficient. These findings provide first-hand observational data for deciphering the sources and transformation mechanisms of regional pollutants. Given the pressing need for finer air quality regulations in the YRD, the synergistic PM and VOC data obtained herein facilitate the precise pinpointing of pollution hotspots and the differentiation of source contributions. This holds

substantial practical significance for advancing joint regional air pollution prevention and elevating the overall efficacy of environmental governance.

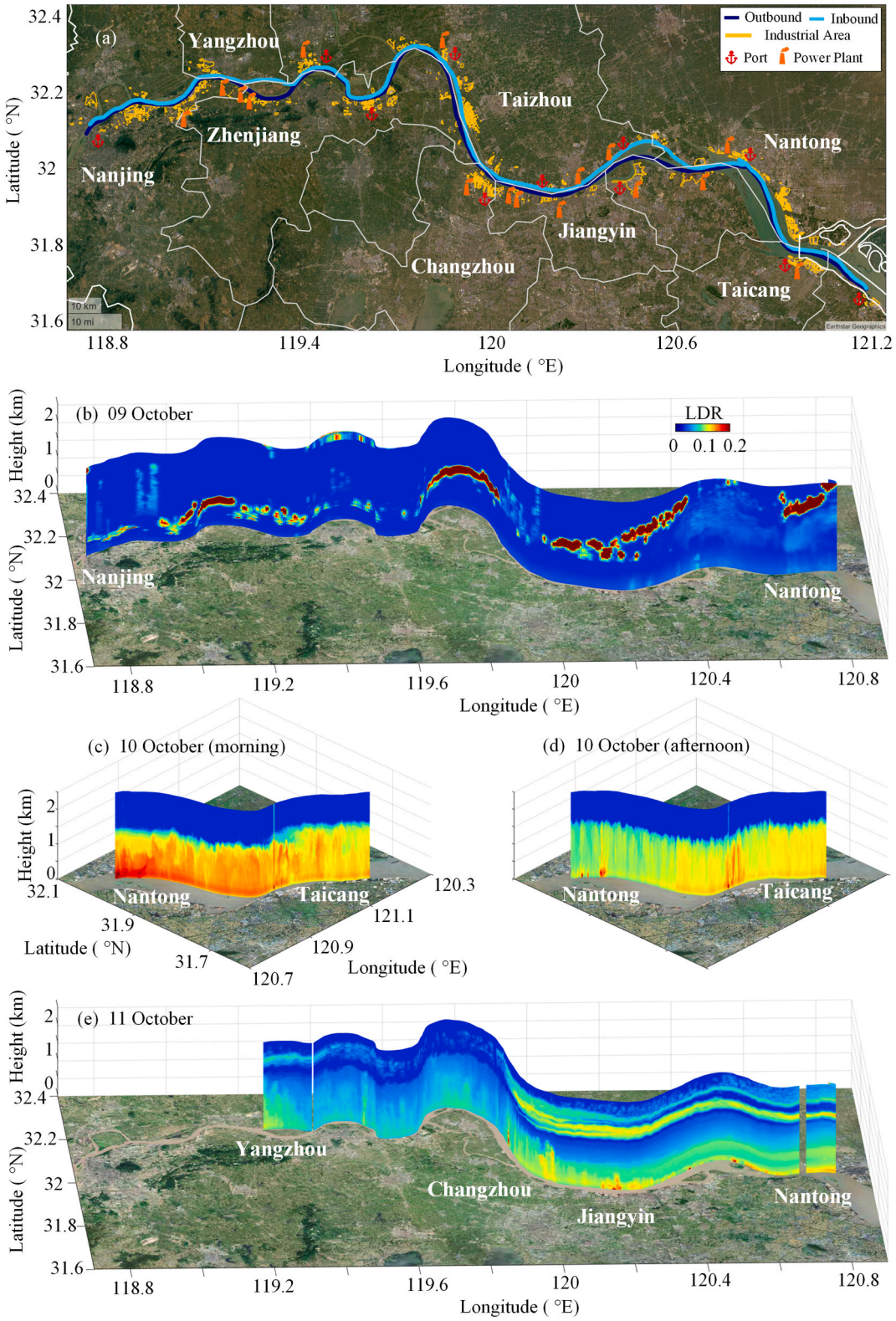

Fig. 1. (a) Shipborne cruise tracks, yellow line shows industrial land use within a 5 km buffer along both sides of Yangtze River. (b) LDR on 9 October (from Nanjing to Nantong); (c) LDR on the morning of 10 October (from Nantong to Taicang); (d) LDR in the afternoon of 10 October (from Taicang to Nantong); (e) LDR on 11 October (from Nantong to Yangzhou).

2. Methodology

2.1. Study area and cruise track

The Jiangsu section of the Yangtze River was selected as the target research area. The shipborne mobile monitoring campaign was conducted from 9 to 11 October 2022. On 9 October, the research vessel departed from Nanjing Port (118.72°E, 32.09°N) at 05:47 and arrived at Nantong Port (120.83°E, 32.01°N) at 17:09. On 10 October, the cruise started from Nantong Port at 09:35, reached Taicang Port (121.18°E, 31.67°N), and then immediately performed an inbound journey, returning to Nantong Port at 14:17. On 11 October, the vessel traveled back from Nantong Port (departure at 05:43) to Nanjing Port, arriving at 18:18. The detailed cruise tracks, along with the locations of major industrial clusters, ports, and power plants along the river, are illustrated in Fig. 1.

2.2. Instruments and data sources

During the monitoring period, a single-photon ionization mass spectrometer (SPIMS-2000) was employed to measure the concentrations and compositions of VOCs in the atmosphere. The SPIMS-2000 offers real-time monitoring with a 5 s time resolution, a mass-to-charge ratio (m/z) coverage of 48–261, sub-ppbv to ppbv level method detection limits (e.g., 0.38–2.46 ppbv for key aromatics) (Mai et al., 2022; Ren et al., 2022), which are critically important for mobile observations (Li et al., 2023; Shang et al., 2022). The spatial sampling density is approximately 28–42 m per data point.

A polarized lidar, operating at a wavelength of 532 nm with a typical pulse energy of 20 mJ and a range resolution of 7.5 m, was used to vertically monitor the LDR of aerosol particles in the air. The vertical extinction coefficient was calculated based on the Fernald method. During shipborne observations, each vertical profile represents a 1-s average, and the horizontal interval between consecutive profiles is approximately 5.6–8.3 m. This horizontal sampling density is sufficient to resolve spatial aerosol variations along the cruise track.

For the ambient environmental data collected during mobile measurements, hourly concentrations of $PM_{2.5}$ and PM_{10} were obtained from national environmental air quality monitoring stations along the Jiangsu section of the Yangtze River. Wind field and relative humidity data were derived from the ERA5 reanalysis dataset provided by the European Centre for Medium-Range Weather Forecasts (ECMWF).

3. Results and discussion

3.1. Polarization lidar observations

During the cruise campaign, the polarization lidar operated in a vertically pointing mode to acquire LDR data. The LDR is defined as the ratio of the perpendicular polarization component to the parallel polarization component in the lidar backscatter signal, with values ranging from 0 to 1. Values approaching 0 indicate that the aerosol particles are highly spherical, whereas higher values suggest more irregular particle shapes. For the 532 nm laser wavelength, the LDR of dust aerosols across various modes does not exceed 0.5, while that of continental aerosols remains below 0.08. Previous studies have established a correlation between particulate matter concentrations and the LDR, demonstrating that the correlation between PM_{10} and the LDR is significantly stronger than that with $PM_{2.5}$ (Wang et al., 2019).

Fig. 1 illustrates the LDR profiles up to 2.5 km during this cruise campaign. The observation results for 9 October are presented in Fig. 1b. Elevated LDR values were observed above most cruise segments that were identified as low-level clouds via lidar detection. Since the laser beam cannot penetrate thick liquid clouds, the light undergoes multiple scattering between liquid cloud droplets, resulting in a rapid increase in the LDR (Sun et al., 2016).

On 10 October, a round-trip cruise observation was conducted between Nantong and Taicang, as depicted in Fig. 1c and d. The ship departed at 09:00 local time (LT). Immediately after leaving Nantong Port, the LDR in the lower boundary layer exceeded 0.2, with high values mainly concentrated below 500 m, whereas the ratios in the middle and upper boundary layer remained below 0.15. Meanwhile, the PM_{10} concentration at the Nantong national environmental air quality monitoring station reached its diurnal peak (Fig. 7). Toward noon, the LDR within the boundary layer gradually decreased, dropping to approximately 0.13 upon arrival at Taicang. As shown in Fig. 1d, the depolarization ratio within the boundary layer further decreased to 0.1 upon arrival back at Nantong.

Fig. 1e illustrates the LDR during the return voyage from Nantong on 11 October. The ship departed at 05:43 LT. Lidar observations revealed a series of high near-surface LDR regions at low altitudes, all of which corresponded to the industrial parks along the Yangtze River. Simultaneously, a high LDR zone exceeding 0.12 was observed at the top of the residual layer at an altitude of 1.7 km, which dissipates when reaching the airspace over Changzhou. After 09:00, significantly elevated near-surface LDR regions were observed in both Changzhou and Jiangyin. Although the high LDR region in Changzhou was overall weaker than that in Jiangyin, its altitude was nearly 500 m higher. Apart from the differences in emission capacities among various industrial parks, this phenomenon is consistent with the diurnal evolution of the planetary boundary layer height (PBLH). No evident high LDR regions were observed during the remainder of the return cruise.

Lidar measurements indicate that elevated LDR values were primarily recorded on 10 and 11 October. Spatially, these high-LDR hotspots were consistently co-located with industrial parks or port terminals, with the most significant enhancements observed near shipyards and port areas.

For instance, while cruising along the northern bank of the Yangtze River between 05:43 and 08:13 LT on 11 October, the vessel traversed a dense cluster of petrochemical and shipbuilding facilities at the Nantong-Taizhou border. Here, the near-surface LDR at a 50-m altitude intermittently spiked above 0.14. Such anomalously high near-surface values during the early morning are unambiguous signatures of strong anthropogenic emissions. Subsequently, from 08:13 to 10:43 LT, the ship passed two major shipyards along the northern bank. Around 09:00 LT, a maximum LDR of 0.16 was detected below 300 m over the first shipyard in northern Jiangyin. About an hour later (around 10:00 LT), a peak LDR of 0.12 was observed over the second shipyard in southeastern Changzhou; remarkably, this high-LDR plume extended up to 800 m.

To further elucidate the atmospheric processes during the cruise, lidar extinction coefficients were incorporated into the analysis. Fig. 2 depicts the temporal evolution of both the extinction coefficient and LDR, and Fig. 3 illustrates the vertical profiles extracted at six representative time points in Fig. 2. As illustrated in Fig. 2, the planetary boundary layer (PBL) on October 9 was characterized by markedly high extinction coefficients coupled with extremely low LDR values, suggesting a clear predominance of spherical particles. Ground-based observations at Nantong (Fig. 7) recorded a sharp daytime surge in $PM_{2.5}$, followed by a delayed nighttime peak in PM_{10}, while strong northwesterly winds (>10 m/s at 925 hPa) prevailed.

On 10 October, the LDR within the PBL remained above 0.1 throughout the day, substantially higher than on 9 October, while the extinction coefficient dropped below 0.075 km^{-1} (Figs. 2 and 3b–e). Both parameters declined gradually over the day. The LDR decreased from around 0.15 to around 0.1, and the extinction coefficient decreased by approximately 0.02 km^{-1}. At the Nantong monitoring station, a pronounced daytime surge in PM_{10} concentrations was recorded. Spatially, enhanced LDR hotspots were consistently observed at three locations during both outbound and return voyages: the departure port terminal, a nearby shipyard, and a mixed emission zone within a riverside industrial park adjacent to the Yangtze River Bridge, which the vessel passed at around 10:30 and around 13:00 LT. Distinct LDR

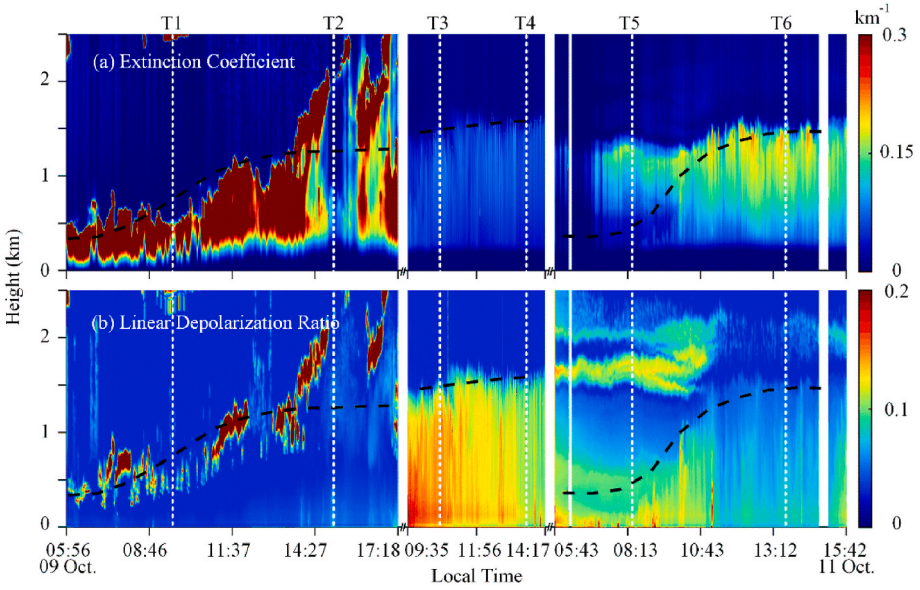

Fig. 2. Lidar-derived aerosol extinction coefficient and LDR. (a) Extinction coefficient; (b) LDR. The PBLH is indicated by the black line.

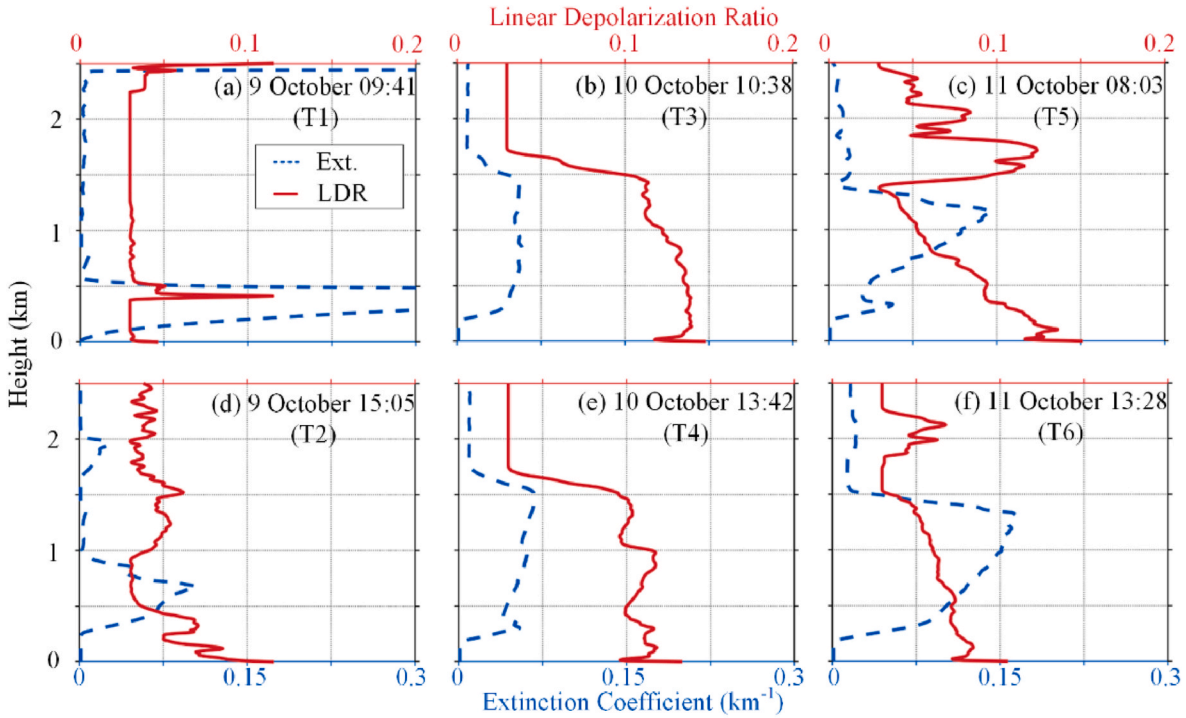

Fig. 3. Detailed vertical profiles at T1–T6 marked in Fig.2. Fig.3 (a,d)09:41 and 15:05 LT on 9 October; (b, e) 10:38 and 13:42 LT on 10 October; (c, f) 08:03 and 13:28 LT on 11 October.

enhancements were captured during both bridge transits, while the extinction coefficient remained largely unchanged.

On 11 October, the observations showed contrasting vertical features (Figs. 2 and 3c–f). During the early morning, the near-surface LDR (below 100 m) exceeded 0.1 and progressively decreased with altitude, while a distinct high-LDR layer (>0.1) about 300 m thick was present between 1.5 and 2.0 km. The extinction coefficient exhibited a negative correlation with LDR: lower near the surface, increasing with altitude, and dropping abruptly above 1.5 km. Relative to 10 October, the layer between 700 and 1500 m showed a depressed LDR combined with an enhanced extinction coefficient. The elevated LDR layer above 1.5 km dissipated by around 11:00 LT. During the afternoon, a substantial enhancement in the extinction coefficient appeared at 1.5 km altitude, while the overall LDR systematically declined.

The spatial coincidence of high near-surface LDR with industrial parks on 11 October demonstrates that these enhancements originate from anthropogenic emissions. The higher altitude reached by the LDR plume over Changzhou compared to Jiangyin (Fig. 1e), despite weaker overall intensity, is consistent with the diurnal evolution of the PBLH and likely modulated by differences in emission strength. The anomalously high near-surface LDR (>0.14) recorded during the early morning passage through the Nantong–Taizhou industrial cluster is an unambiguous signature of strong primary emissions. For the two shipyards, the higher vertical dispersion of the Changzhou plume (up to 800 m),

despite the smaller scale of the facility, can be explained by the combined effect of a deeper PBL later in the morning and favorable local dispersion conditions induced by a nearby cross-river bridge.

3.2. VOCs observations

VOCs are recognized as critical precursors of SOA. Given the high density of chemical industrial parks situated along both banks of the Yangtze River, synchronized measurements of VOC concentrations were conducted throughout the cruise observation. Fig. 4 illustrates the temporal variations in TVOC concentrations. Based on the spatial distribution of the cruise track, the observation period was partitioned into six symmetrical time episodes. Table 1 summarizes the dominant VOC species and their respective mass fractions for the first five episodes, with the corresponding chemical compositions further visualized in Fig. 5. To specifically characterize the heavily polluted regions, data points with TVOC concentrations below 10 ppbv were excluded from the analysis for these specified episodes.

The toluene-to-benzene (T/B) ratio is a widely utilized diagnostic tool for discriminating between vehicular and non-vehicular emission sources. T/B ratios within the range of 0.6–1.0 are generally considered characteristic signatures of typical motor vehicle exhaust. In contrast, ratios exceeding 2.0 serve as a robust indicator of solvent evaporation or industrial activities, as toluene is extensively employed as a solvent in coatings, printing processes, adhesives, and chemical manufacturing (Gelencsér et al., 1997; Li et al., 2020; Sun et al., 2016). Furthermore, owing to the higher photochemical reactivity of toluene compared to benzene, the magnitude of the T/B ratio also acts as a proxy for the photochemical age or "freshness" of the sampled air mass (Yuan et al., 2013; Zou et al., 2023).

Significant VOC enhancements were recorded during the middle segment of the outbound leg (Episode 1); however, such emissions were largely absent during the corresponding return journey (Episode 6). Due to the absence of obvious VOCs pollution in Episode 6, the subsequent analysis only examines Episodes 1-5. Analysis of the T/B diagnostic ratio reveals that the values in Episode 1 were markedly lower than those in Episodes 2–4, yet remained higher than in Episode 5.

To quantitatively evaluate the potential influence of diurnal photochemical variations on the observed VOC differences, we extracted the hourly surface solar radiation downwards from the ERA5-Land reanalysis dataset and calculated the domain-averaged instantaneous irradiance over the study region (118–122°E, 31–33.5°N) for both 9 October and 11 October (Fig. A.3). The results show that the irradiance on 11 October was higher than that on 9 October by approximately 100 W/m^2. We acknowledge that photochemistry does affect VOC concentrations, with higher irradiance generally accelerating their consumption (e.g., peak VOCs in Episode 2 vs. Episode 5). However, the compositional shifts between episodes contradict a photochemistry-dominated interpretation. As shown in Fig. 5, Episode 2 is dominated by alkanes, whereas Episode 5 exhibits a much higher fraction of aromatics—species that react far faster with ·OH radicals. Under stronger photochemical conditions (higher irradiance on 11 October), one would expect the more reactive aromatics to be preferentially depleted. The fact that the aromatic fraction increased rather than decreased suggests that photochemical loss alone cannot explain the observed compositional differences. Moreover, the ~100 W/m^2 irradiance increase between 9 and 11 October is insufficient to account for the near-complete disappearance of VOCs in Episode 6. Instead, the decisive factor is the marked shift in wind field (Fig. A.1b, h): strong northwesterly winds on 9 October transported pollutant plumes into the cruise track, whereas stagnant northeasterly winds on 11 October largely suppressed regional transport and local accumulation.

This specific T/B ratio pattern indicates that the observed pollution was primarily driven by the transport of an aged air mass. From a meteorological perspective, the robust northwesterly winds on 9 October served as a primary driver, not only transporting aerosol plumes but also likely advecting upwind VOC precursors across the river surface.

The VOC composition in Episode 2 was comparable to that in Episode 1, with halogenated hydrocarbons remaining the predominant species in both segments. However, Episode 2 exhibited a significant enhancement in the T/B ratio, accompanied by a higher mass fraction of aromatic hydrocarbons. Specific species identification provided further insights

Table 1
Concentration and proportion of dominant VOCs species in each pollution period.

Episode	T/B Ratio	VOC Species	Concentration (ppbv)	Fraction
Episode 1	2.74	Trichloroethane	3.303	13.0%
		Trimethylbenzene	3.093	12.2%
		1,1-Dichloroethylene	2.209	8.7%
		Xylenes & Ethylbenzene	1.690	6.6%
		1,1,2,2-tetrachloroethane (1,1,2,2-TeCA)	1.543	6.1%
Episode 2	6.67	Trichloroethane	6.156	16.6%
		Trimethylbenzene	3.825	10.3%
		Xylenes & Ethylbenzene	3.546	9.6%
		Diethylbenzene	3.195	8.6%
		1,1,2,2-TeCA	2.954	8.0%
Episode 3	4.82	Trichloroethane	12.828	21.1%
		1,1,2,2-TeCA	5.769	9.5%
		Diethylbenzene	5.561	9.2%
		1,1-Dichloroethylene	4.309	7.1%
		Trimethylbenzene	4.184	6.9%
Episode 4	9.68	1,1-Dichloroethylene	6.971	11%
		Diethylbenzene	4.972	7.8%
		Xylenes & Ethylbenzene	3.965	6.2%
		n-Decane	3.664	5.8%
		1,3-Dichloropropene	3.433	5.4%
Episode 5	1.48	Xylenes & Ethylbenzene	9.114	36.0%
		Diethylbenzene	2.030	8.0%
		Pentene	1.929	7.6%
		Toluene	1.444	5.7%
		Trimethylbenzene	1.369	5.4%

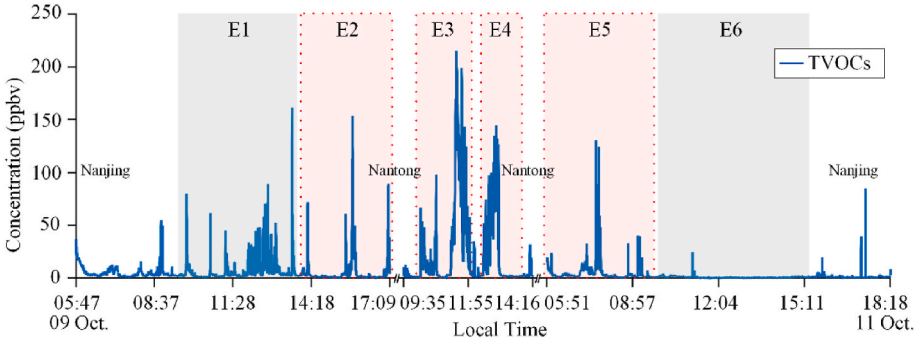

Fig. 4. Variations in TVOCs concentrations.

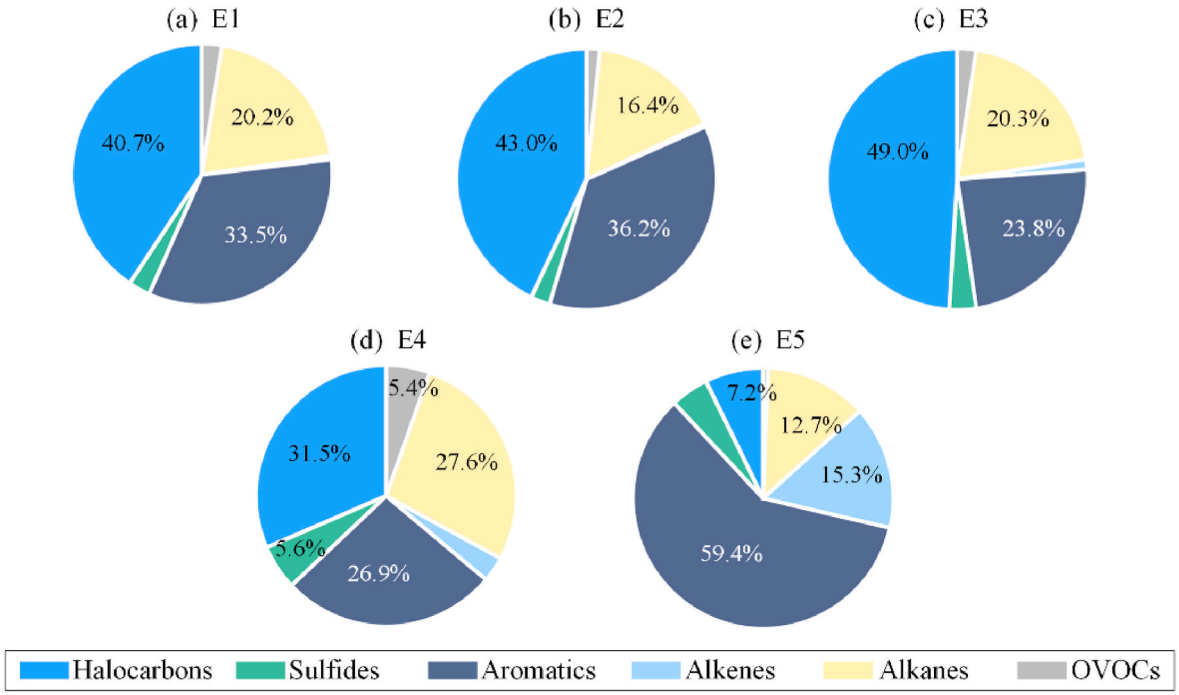

Fig. 5. VOCs species proportion during each episode.

into the emission sources. Trichloroethane, characterized by its exceptional organic dissolution capacity and relatively low toxicity, has been extensively utilized as a cleaning solvent in the aviation, automotive, and electronics industries. Additionally, it serves as a solvent for water- and oil-repellent treatments in paper and textiles, and is a known constituent in certain pesticide formulations (Doherty, 2000). Similarly, tetrachloroethane—sharing comparable chemical properties with trichloroethane—is frequently detected in emissions from the plastics industry (Shao, 2019). Furthermore, trimethylbenzene and 1, 1-dichloroethylene are primarily employed as raw materials for coating production. This specific cruise segment navigated past a vast cluster of industrial parks along the northern bank of the Yangtze River, which are dominated by port facilities, material chemicals, and textile dyeing industries. Consequently, the pollution characteristics observed in Episodes 1 and 2 can be attributed to the superposition of regional transport from upstream areas and localized industrial emissions along the riverbanks.

In Episode 3, 1,1,1-trichloroethane emerged as a dominant species, accounting for 21.1% of the total VOCs. This segment was further characterized by the enrichment of highly stable halogenated hydrocarbons and long-chain substituted aromatics, such as 1,1,2,2-tetrachloroethane and diethylbenzene, with the total volume fraction of halogenated hydrocarbons reaching 49%. Due to chlorine's electron-withdrawing and steric effects, chlorinated alkanes exhibit OH rate constants ($\sim 10^{-14}$ cm^3 $molecule^{-1}$ s^{-1}) two orders of magnitude lower than aromatics ($\sim 10^{-12}$) (Atkinson and Arey, 2003), resulting in atmospheric lifetimes of months or longer. Due to their chemical inertness and sluggish photochemical degradation rates, the prevalence of these halocarbons signifies persistent industrial inputs and minimal air mass aging, reflecting a strong and consistent contribution from local chemical sources.

Episode 4 exhibited the highest T/B ratio among all observed periods. While the proportion of halogenated hydrocarbons declined, the abundance of alkanes rose to 27.6%. Notably, n-decane was a key component, a long-chain alkane typically associated with petrochemical facilities or ship engine exhaust. This episode was predominantly governed by solvent evaporation, fugitive emissions of chemical feedstocks, and petrochemical-related volatilization. The distinct simplification of the aromatic profile, coupled with the negligible influence of regional transport or photochemical processing, underscores that this air mass represents a typical fresh industrial plume originating from proximal sources.

In Episode 5, the T/B ratio declined to a relatively low level of 1.48. This segment was characterized by a substantial mass fraction of xylene and ethylbenzene (combined 36%), the detection of olefins such as pentene, and a sharp increase in aromatic hydrocarbons to 59.4%, whereas the contribution from halogenated hydrocarbons significantly diminished. These chemical signatures are consistent with the T/B characteristics typically associated with motor vehicle exhaust and fossil fuel combustion. Notably, although Episodes 2 and 5 are spatially proximal, their VOC compositions and dominant species exhibited distinct discrepancies. This can be explained by the meteorological transition on 11 October, during which mid-to-high altitude wind speeds decreased markedly and the wind field shifted to weak northeasterly. Based on satellite imagery, the pollution peaks recorded during Episode 5 consistently corresponded to the locations of port terminals and shipyards. Consequently, the VOCs measured during this period likely originated from a combination of ship emissions and shipbuilding-related industrial activities along the Yangtze River. Previous studies have shown that aromatic hydrocarbons emitted by ships in port are dominated by benzene, toluene, ethylbenzene, and xylene (BTEX) (Xiao et al., 2018). Given that xylene and ethylbenzene are also primary constituents of industrial paints (Ghobakhloo et al., 2023), their abundance is further linked to the open-air spray painting processes prevalent in shipyards. Additionally, slight enhancements in TVOC concentrations were observed at the commencement and conclusion of each daily observation, further underscoring the persistent influence of VOC emissions from port areas. As no notable VOC enhancements were detected during Episode 6, this period was not included in the subsequent detailed compositional and source analyses.

Building upon the preceding analysis of VOC chemical composition and source apportionment along the cruise track, this study further evaluated the secondary organic aerosol formation potential (SOAP) of key VOC species for each episode. The SOAP was employed to characterize the aerosol formation capacity of VOCs. In this study, the toluene equivalent mass method (Derwent et al., 2010) was applied. This

method reflects the propensity of individual organic compounds to form SOA on an equal mass basis relative to toluene, which is represented by the SOAP index. The secondary organic aerosol potential for each specific organic compound ($SOAP_i$) were calculated as follows:

$$SOAP_i = \frac{Increment\ in\ SOA\ mass\ concentration\ with\ species, i}{Increment\ in\ SOA\ with\ toluene} \times 100 \quad (1)$$

The $SOAP_i$ values utilized in this study were referenced from Derwent et al. (2010). The total SOAP is derived by multiplying the $SOAP_i$ by the mass concentration of the corresponding VOC species (c_i), calculated as follows:

$$SOAP = \sum c_i \times SOAP_i \quad (2)$$

The results are presented in Fig. 6. Throughout the observation period, the total SOAP (ΣSOAP) for the five identified pollution episodes exhibited pronounced variability, ranging from 15.01 to 51.72 μg/m^3.

For Episodes 1 and 2, the ΣSOAP values were recorded at 19.99 μg/m^3 and 28.30 μg/m^3, respectively. xylene/ethylbenzene and toluene emerged as the predominant contributors, collectively accounting for over 70% of the total SOAP. This dominance is in close alignment with the characteristic benzene series profiles associated with industrial solvent emissions during these periods. These findings underscore that industry-related aromatic VOCs serve as crucial precursors driving SOA formation in the upstream regions.

The SOAP characteristics during the two episodes within the core pollution zone exhibited distinct discrepancies. In Episode 3, the ΣSOAP reached its minimum value (15.01 μg/m^3) across the entire observation period. Trimethylbenzene, dodecane, and undecane were identified as the primary contributors. This pattern closely mirrors the emission fingerprints characterized by the absolute dominance of halogenated hydrocarbons (e.g., trichloroethane and 1,1,2,2-tetrachloroethane), which possess lower SOAP potentials. The minimal contribution of these halocarbons to SOA formation resulted in a suppressed overall SOAP level during this period. By contrast, the ΣSOAP in Episode 4 surged to 39.49 μg/m^3. This substantial increase was driven by the significantly enhanced contributions of xylene/ethylbenzene and toluene, which emerged as the top two SOAP contributors. These variations reflect a marked increase in the mass fraction of highly reactive aromatics originating from proximal industrial emissions, thereby leading to a concomitant elevation in the regional SOA formation potential.

During Episode 5, which was characterized by a dominance of traffic sources in the downstream symmetrical region, the ΣSOAP reached its peak value of 51.72 μg/m^3 for the entire observation period. Within this episode, the contribution of xylene/ethylbenzene was overwhelmingly dominant, accounting for nearly 40 μg/m^3, followed by toluene. The mass fraction of xylene/ethylbenzene reached 36% of the total VOCs, which is highly consistent with the emission signatures of industrial solvents. Furthermore, the T/B ratio aligned well with the characteristics of traffic-related sources, such as engine exhaust. These results underscore that highly reactive aromatics originating from both industrial

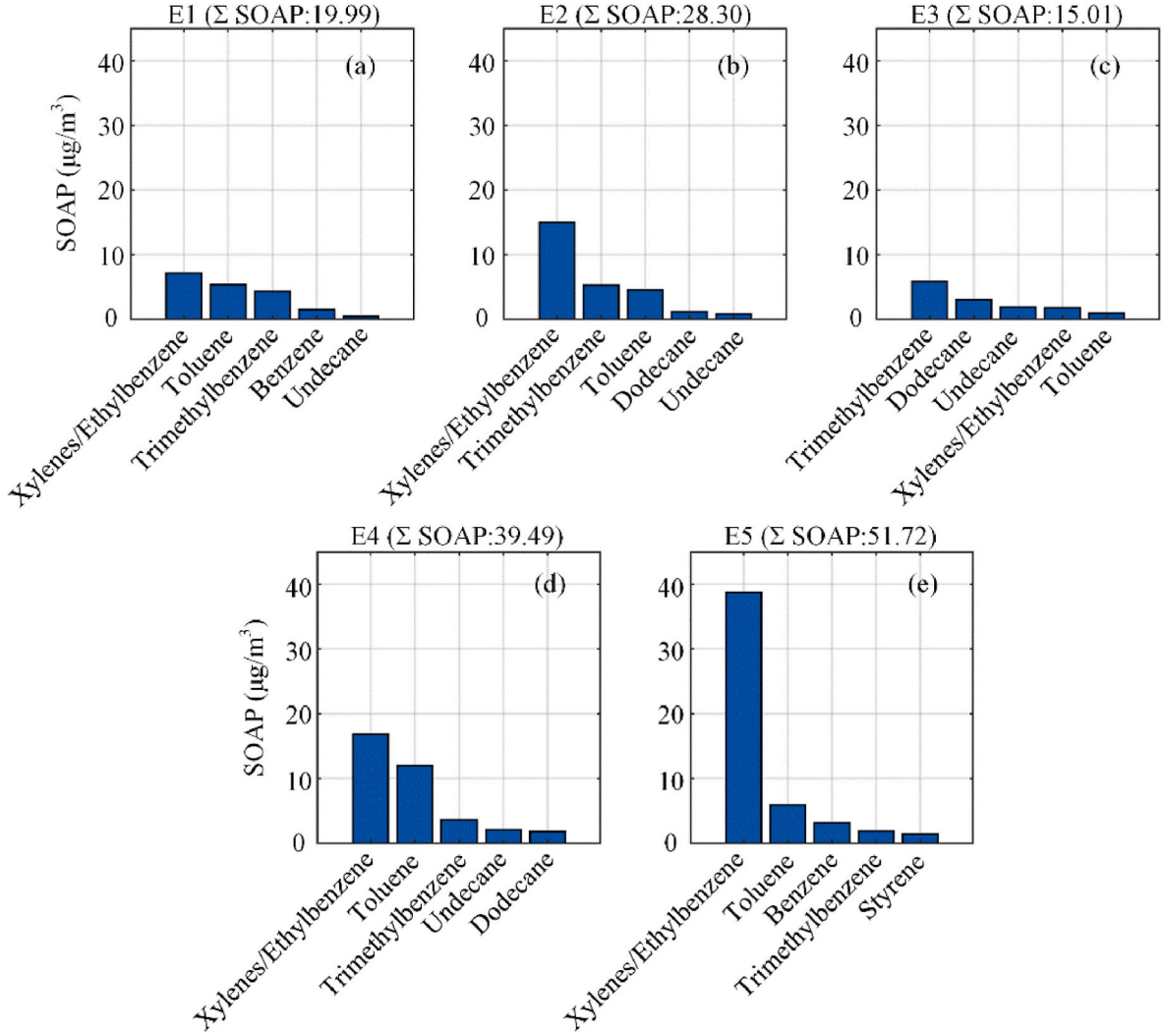

Fig. 6. Top five species with the highest SOAP contributions in each episode.

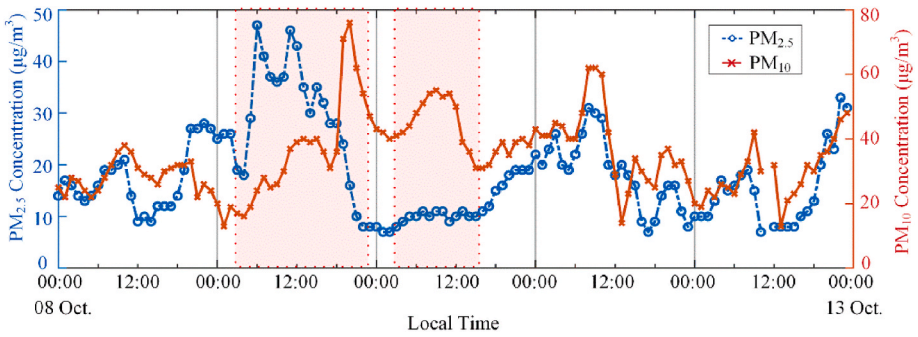

Fig. 7. Changes of $PM_{2.5}$ and PM_{10} concentration in Nantong station (120.86 °E, 32.00 °N) from 8 to 12 October by national environmental air quality monitoring stations.

solvents and traffic emissions are the core drivers of SOA formation in the downstream region. During this period, the meteorological conditions were relatively stagnant, which, coinciding with the lidar observations of aerosol aging within the boundary layer, facilitated the intensive chemical transformation of precursors into secondary organic aerosols.

Overall, the SOA formation potential across the study area exhibited pronounced temporal variability. While industrial emissions dominated by halogenated hydrocarbons exerted a constrained influence on SOA production, industrial solvent sources and traffic-related combustion—characterized by an abundance of highly reactive aromatics—emerged as the primary drivers of SOA formation. Notably, species such as xylene and ethylbenzene originating from traffic emissions displayed exceptionally high SOAP, underscoring their substantial and non-negligible role in regional secondary organic aerosol pollution.

3.3. Large-scale particulate matter transport process

A large-scale aerosol transport process was captured during the cruise monitoring. By synthesizing the variations in $PM_{2.5}$ and PM_{10} with concurrent meteorological data. The pollution observed on 9 October came from nearby regional transport, while the pollution on 10 October came from dust aerosols in the Mongolian region.

Fig. 7 presents the concentration profiles of $PM_{2.5}$ and PM_{10} at the Nantong national monitoring station (120.86°E, 32.00°N) from 8 to 12 October. On 9 October, the $PM_{2.5}$ concentration exhibited an anomalous "M-shaped" profile with extremely low values during the nighttime. $PM_{2.5}$ concentrations surged after 05:00 LT on 9 October, synchronized with high northwesterly wind speeds at 925 hPa. The peaks of "M-shaped" structure occurred at 10:00 and 12:00 LT. After 20:00 LT, concentrations plummeted to below 10 μg/m^3 and remained low until midnight. Concurrently, PM_{10} levels underwent a rapid surge and subsequent decline at night. These variations deviated significantly from typical autumnal diurnal trends.

From 09:00 to 14:00 LT on 10 October, the RH across the region remained below 60% (Fig. A.2). Under the influence of persistent northwesterly winds, $PM_{2.5}$ concentrations showed a gradual increase, whereas PM_{10} reached its diurnal peak at 09:00 LT before progressively declining. Considering that the $PM_{2.5}$ concentrations at most stations are at extremely low levels (Fig. A.1.), the episode was identified as a north-to-south regional particulate matter transport event.

Fig. 8 simulates the 72-h backward trajectories at 500 m, 1000 m, and 1500 m above the surface at Nantong Station at 09:00 LT on 10 October. The results show that air masses at 500 m and 1500 m originated from the upper levels of Mongolia, while those at 1000 m came from the surface of Inner Mongolia. This transport evolution is further supported by the 72-h trajectory cluster analysis (Fig. A.4). By 11 October, the air mass pathways transitioned significantly into northeastern and coastal recirculating flows (dominated by clusters of 41.67% and 37.50%), reflecting a weakened long-range propulsion. The dust

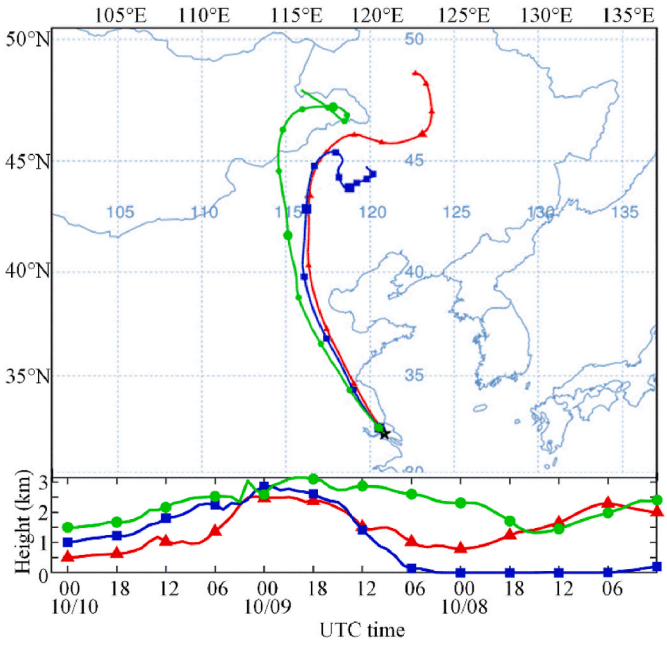

Fig. 8. Simulation results of backward trajectories at 500 m, 1000 m and 1500 m above the Nantong station (120.86 °E, 32.00 °N), starting at 01:00 UTC on 10 October (09:00 LT on 10 October).

was lifted at 06:00 LT on 8 October and then transported over Nantong. This attenuation process was effectively captured by polarization lidar observations. A clear reduction in the LDR is visible in Fig. 1c and d, further corroborating the settling or dispersion of coarse particles.

On 11 October, the wind field shifted to northeasterly, marking a transition in air mass origin from inland regions to the East China Sea. Driven by an east-to-west spatial gradient of increasing RH, $PM_{2.5}$ concentrations rose across the stations in Yangzhou, Taizhou, and Changzhou (Fig. A.1). Simultaneously, synchronized high peaks of both $PM_{2.5}$ and PM_{10} were recorded at the Nantong monitoring station (Fig. 7).

3.4. Discussion

3.4.1. Regional transport and aging of aerosols

Based on shipborne lidar observations, this section elaborates the aerosol evolution over the Yangtze River Jiangsu section during 9 to 11 October, covering three typical successive processes: regional transport of aged anthropogenic aerosols, dust-polluted mixed aerosol intrusion, and continuous photochemical aging accompanied by local pollutant emissions.

The high extinction coefficients together with very low LDR on 9

October point to a predominance of spherical particles. This optical pattern, together with the observed $PM_{2.5}$ surge, delayed PM_{10} peak, and strong northwesterly winds, explicitly points to a north-to-south regional pollution transport event. In the transported air mass, finer and lighter $PM_{2.5}$ reached the Yangtze River first, while the coarser PM_{10} fraction arrived hours later. High extinction combined with low LDR is a well-recognized signature of polluted aerosols; although many anthropogenic particles are non-spherical at emission, atmospheric aging driven by photochemical processes gradually renders them more spherical, thereby reducing the LDR (Baars et al., 2019; Fan et al., 2018). The strong confinement of the aerosol layer within the PBL further supports its polluted nature (Huang et al., 2012). Therefore, the 9 October episode is interpreted as a typical case of northerly wind-driven regional transport that initially delivered aged, spherical $PM_{2.5}$ particles.

On 10 October, the combination of persistently elevated LDR (>0.1) and substantially reduced extinction coefficient (<0.075 km^{-1}) differs markedly from the polluted episode of the previous day. Although the maximum LDR did not reach the around 0.25 typical of pure dust, the optical pairing of relatively high LDR and low extinction is widely employed as a robust criterion for dust or dust–pollution mixed aerosols (de Foy et al., 2011; Panahifar et al., 2020; Zhou et al., 2013). This interpretation is corroborated by the concurrent daytime PM_{10} surge at Nantong. The localized LDR enhancements observed near the port terminal, shipyard, and bridge-associated industrial zone, with minimal variation in extinction, are likely attributable to primary anthropogenic emissions from industrial operations or bridge traffic.

The vertical structure on 11 October captures a transition from dust-polluted mixed aerosols to aged and secondary organic aerosols. The reduction in LDR observed between 700 and 1500 m, accompanied by an increased extinction coefficient relative to 10 October, is a well-established indicator of aerosol aging (Burton et al., 2012). This suggests that aerosols trapped in the nocturnal residual layer over the Yangtze River underwent significant aging, leading to a higher fraction of spherical particles. The elevated high-LDR layer above 1.5 km is ascribed to the dust-polluted mixed aerosols advected on 10 October, likely sustained by a nocturnal temperature inversion that suppressed gravitational settling. This aloft layer persisted under clear-sky conditions (RH < 60% on 10 October, RH < 80% on 11 October, Fig. A.2) and exhibited both moderate LDR values (0.10–0.20) and low extinction coefficients, thereby ruling out the possibility of cloud contamination or low-level clouds. The dissipation of this aerosol layer by around 11:00 LT is consistent with the post-sunrise development of the PBL, enhanced convective mixing, and the vessel moving away from the primary source region. In the afternoon, the substantial extinction enhancement at 1.5 km, concurrent with a systematic LDR decline, points toward active secondary aerosol formation. Given the intense solar radiation, it is plausible that reactive precursors within the PBL were transported upward by turbulent diffusion and underwent intensive photochemical reactions with the advected dust-polluted aerosols near the PBL top, thereby accelerating further aging and facilitating the formation of secondary aerosols.

3.4.2. VOCs compositional characteristics and its effects on aerosol evolution

High-resolution shipborne VOC observations reveal distinct compositional differences and source signatures across various pollution episodes along the river. Combined with aerosol optical evolution results from polarization lidar, this section further explores the linkage between different VOC emission sources and the atmospheric aging as well as secondary formation of regional aerosols.

High spatiotemporal resolution VOC measurements along the cruise track suggest that emissions from industrial parks on both banks of the Yangtze River and from shipping activities likely played a substantial role in shaping the observed aerosol pollution. Episode 1 was dominated by halogenated hydrocarbons from aged, regionally transported air masses; Episode 2 reflected a mix of regional transport and local industrial solvent use, with elevated aromatics and trichloroethane; Episode 3 was characterized by persistent fresh emissions from nearby chemical industries, overwhelmingly enriched in 1,1,1-trichloroethane and other inert halocarbons; Episode 4 featured fresh petrochemical and engine-related plumes, with increased alkanes such as n-decane; Episode 5 was dominated by ship and shipyard emissions, with exceptionally high fractions of xylene and ethylbenzene alongside BTEX; and Episode 6 showed negligible VOC enhancements, indicating minimal local source impacts along the return track.

When these VOC constraints are considered alongside the lidar-derived optical evolution, a more complete, albeit tentative, interpretation emerges for 11 October. The morning vertical structure captured a transition from residual dust-polluted mixed aerosols to an aging aerosol layer, as suggested by the declining LDR and increasing extinction between 700 m and 1500 m. As boundary layer growth and enhanced convective mixing occurred, it is reasonable to infer that highly reactive aromatics from local ship and industrial emissions, as illustrated by the extreme SOAP observed in Episode 5, were transported upward and experienced photochemical processing near the PBL top. This episode is broadly consistent with the afternoon enhancement of extinction at around 1.5 km and the concurrent systematic decline in LDR, previously interpreted as a signature of active secondary organic aerosol formation. These coincidences therefore suggest that the high SOAP from local anthropogenic VOCs, combined with the stagnant meteorological conditions and diurnal boundary-layer dynamics, may have contributed significantly to the secondary aerosol formation episode observed on the third day, though the relative importance of this local precursor supply versus other processes remains to be quantified.

4. Conclusion

Building upon the synergistic observations along the Jiangsu section of the Yangtze River, this study elucidates the distinct air pollution evolution patterns and underlying physicochemical mechanisms of this critical waterway. Three typical aerosol evolution episodes were identified, which were closely regulated by meteorological parameters: under prevailing northwesterly winds on 9 October, a significant north-to-south regional transport event occurred, with aerosols dominated by aged spherical particles characterized by high extinction and low LDR; on 10 October, under strong northwesterly winds conditions, dust-mixed aerosols were captured, exhibiting markedly elevated LDR over port terminals and industrial zones; by 11 October, under stagnant northeasterly winds, dust-mixed aerosols experienced continuous aging evolution, driven by local emissions and daytime planetary boundary layer activities. Simultaneously, VOC concentrations exhibited pronounced spatiotemporal heterogeneity, with dominant species diverging according to emission sources. High-pollution episodes were mainly affected by emissions from riverside chemical industries and solvent volatilization, and such pollution sources are predominated by halogenated hydrocarbons and substituted aromatics. Xylene and ethylbenzene showed prominent enrichment levels in partial navigation segments with a maximum proportion of 36%, which reveals the considerable pollution contributions derived from ship activities and port operations.

Further SOAP evaluations confirmed that highly reactive aromatics serve as the core precursors driving regional SOA formation, whereas the contribution of chemically inert halogenated hydrocarbons remains constrained, reflecting a high degree of coupling between SOAP characteristics and emission source profiles. Future attention should be continuously paid to VOC emissions from industrial parks and open-air shipbuilding facilities along both banks of the Yangtze River.

In conclusion, air pollution along the Yangtze River is fundamentally driven by the superposition of riverside industrial emissions and maritime traffic, presenting unique spatiotemporal and compositional patterns that distinguish it from typical urban environments. These findings clarify the source-receptor relationships and meteorological regulatory

mechanisms in this region, providing a robust scientific basis for refined air quality management and integrated pollution control strategies across the Yangtze River Delta.

CRediT authorship contribution statement

Yixiang Chen: Writing – original draft, Visualization, Methodology, Investigation, Formal analysis, Conceptualization. **Ming Ding:** Investigation, Data curation. **Zhen Zhang:** Writing – review & editing, Supervision, Formal analysis. **Saifen Yu:** Writing – review & editing, Formal analysis. **Qiuwei Xia:** Writing – review & editing. **Daihao Yu:** Writing – review & editing. **Jiawei Yang:** Writing – review & editing. **Haiyun Xia:** Supervision, Resources, Data curation.

Financial support

This study has been supported by the National Natural Science Foundation of China (42405138, 42305147), Natural Science Foundation of Jiangsu Province (BK20230428).

Declaration of competing interest

The authors declare the following financial interests/personal relationships which may be considered as potential competing interests: Zhen Zhang reports financial support was provided by National Natural Science Foundation of China. Zhen Zhang reports financial support was provided by Natural Science Foundation of Jiangsu Province. If there are other authors, they declare that they have no known competing financial interests or personal relationships that could have appeared to influence the work reported in this paper.

Acknowledgement

We acknowledge the High Performance Computing Platform of Nanjing University of Information Science & Technology for their support of this work. We also thank Bing Maps for providing remote sensing map services. We are grateful to Xiaolei Wang for collecting and compiling the Air Quality Index data of China's environmental monitoring stations(https://quotsoft.net/air/). We further acknowledge the Jiangsu Provincial Environmental Monitoring Center for organizing this shipborne observation campaign and sharing relevant monitoring data.

Appendix A

A region-wide shift in PM concentrations was captured during the cruise monitoring. By synthesizing the variations in $PM_{2.5}$ and PM_{10} with concurrent meteorological data (wind field and relative humidity), the event was attributed to a large-scale aerosol transport process. The underlying characteristics and drivers of these variations are further analyzed below.

Fig. A.1. illustrates the synoptic wind field at 925 hPa and the concurrent variations in $PM_{2.5}$ concentrations at surrounding national monitoring stations during the cruise. On 9 October (Fig. A.1a–c), at 06:00 LT, northwesterly winds (around 12 m/s) prevailed in the Nanjing–Yangzhou region, while westerly winds of similar intensity were observed near Changzhou, Taizhou, and Nantong. Concurrently, $PM_{2.5}$ concentrations began to rise in several cities. By 12:00 LT, the wind field across the Jiangsu section of the Yangtze River had shifted entirely to northwesterly, with speeds slightly increasing up to 15 m/s. Under the influence of persistent northwesterly winds, $PM_{2.5}$ levels declined in most cities, although upward trends persisted at some stations in Nantong. By 18:00 LT, the wind further veered northward and weakened slightly; consequently, $PM_{2.5}$ concentrations at most stations remained lower than their morning peaks, with the exception of Changzhou and northern Wuxi.

Regarding 10 October (Fig. A.1d–f), wind speeds remained stable at 8–10 m/s, with the direction gradually transitioning from northwesterly to northly. Regional $PM_{2.5}$ concentrations remained notably low (<20 $\mu g/m^3$) throughout the day.

On 11 October (Fig. A.1g–i), the wind field shifted to northeasterly and wind speeds decreased significantly. Stagnant conditions were observed within the boundary layer near Nanjing and Yangzhou, while wind speeds near Nantong were maintained at around 4 m/s, leading to relatively high $PM_{2.5}$ levels at several stations in Yangzhou, Taizhou, and Changzhou. By 14:00 LT, as the vessel traversed the Zhenjiang section, the wind shifted to easterly and speeds near Yangzhou increased to around 4 m/s, causing $PM_{2.5}$ concentrations at national stations to drop below 30 $\mu g/m^3$. By 16:00 LT, the wind further transitioned to southeasterly near Nanjing, coinciding with rising $PM_{2.5}$ levels at some stations in Wuxi. Notably, as the Yangtze River banks are densely lined with port terminals and industrial parks, most national monitoring stations are situated in urban or suburban areas at considerable distances from the main river channel. Therefore, data from these stations primarily serve as a regional reference for the spatiotemporal trends of $PM_{2.5}$ rather than a precise reflection of the immediate cruise environment.

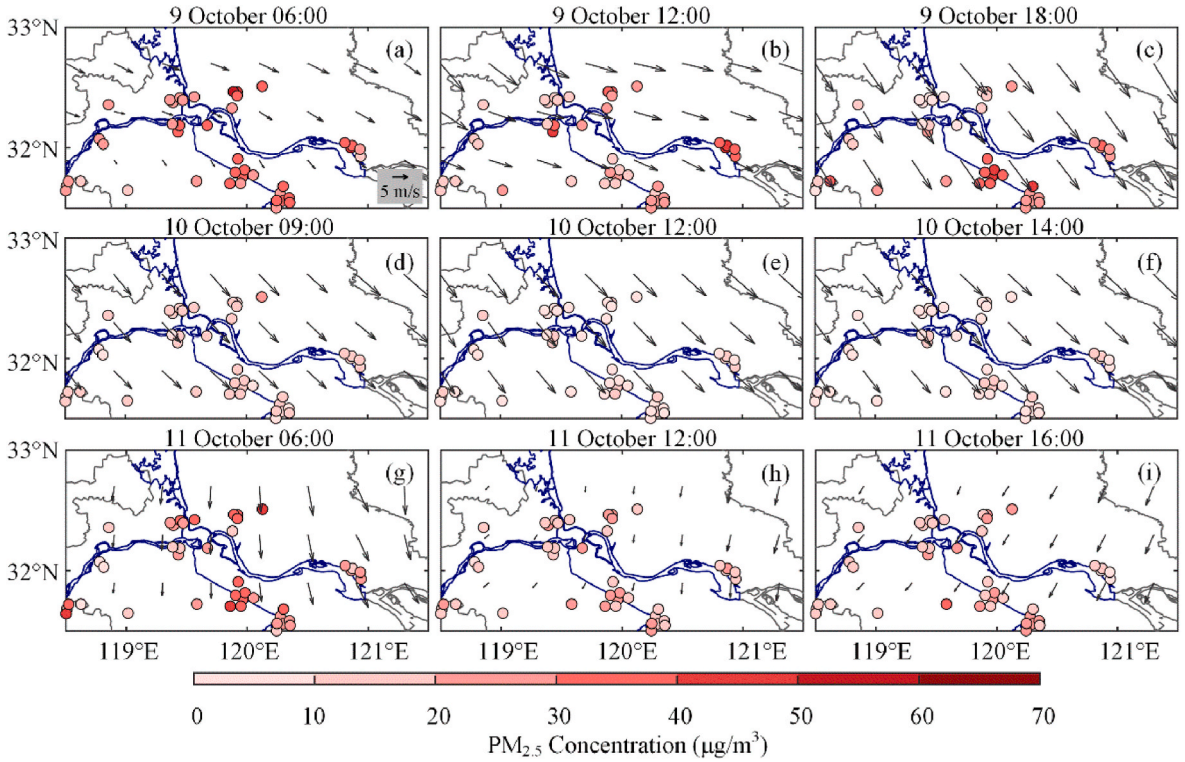

Fig. A.1. Monitoring route of 9 to 11 October, the dots represent the national environmental air quality monitoring stations, the color of dots indicates the concentration of $PM_{2.5}$, and the 925 hPa wind field is from ERA5 reanalysis data.

Fig. A.2 further illustrates the spatiotemporal evolution of relative humidity (RH) at 925 hPa during the cruise. At 06:00 LT on 9 October, RH exceeded 85% in certain areas under cloudy morning conditions; however, it subsequently dropped below 60% across most regions, driven by persistent northwesterly winds. Dominated by northly winds on 10 October, the RH remained below 60% throughout the day. With the wind turning northeasterly on 11 October, relative humidity rose progressively from east to west.

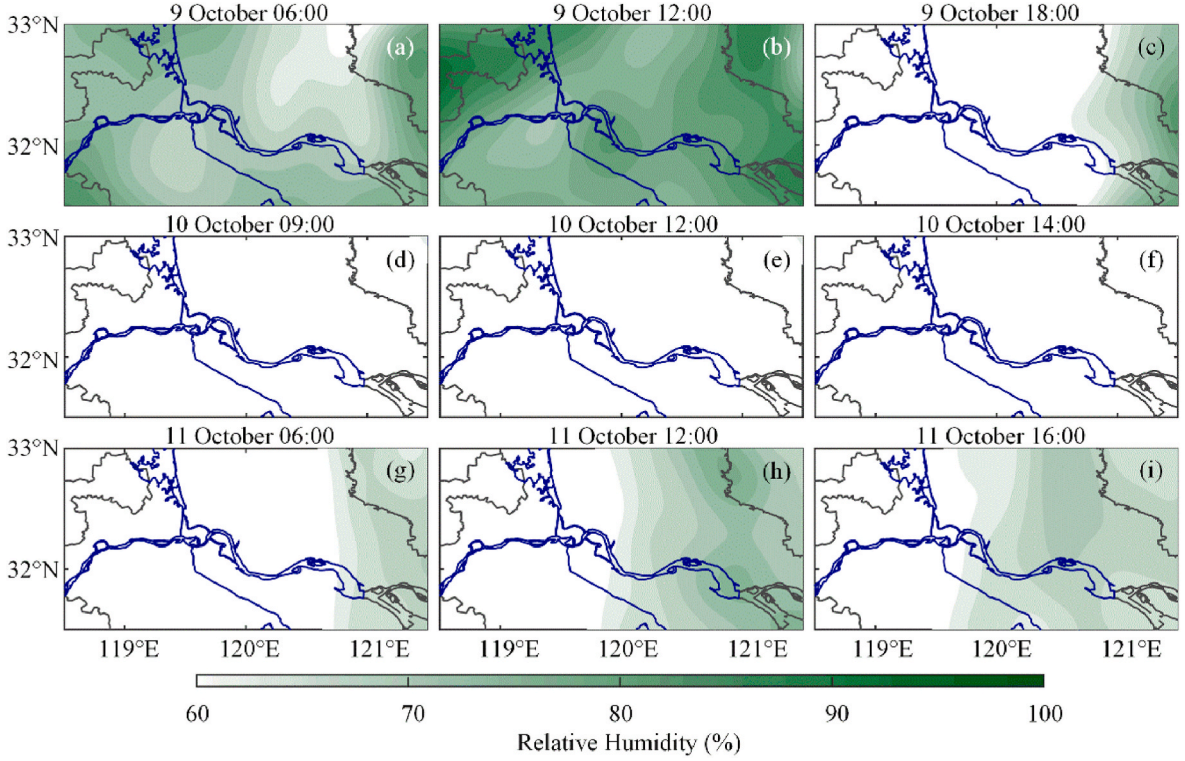

Fig. A.2. Variation of RH in the Monitoring Area from 09 to 11 October.

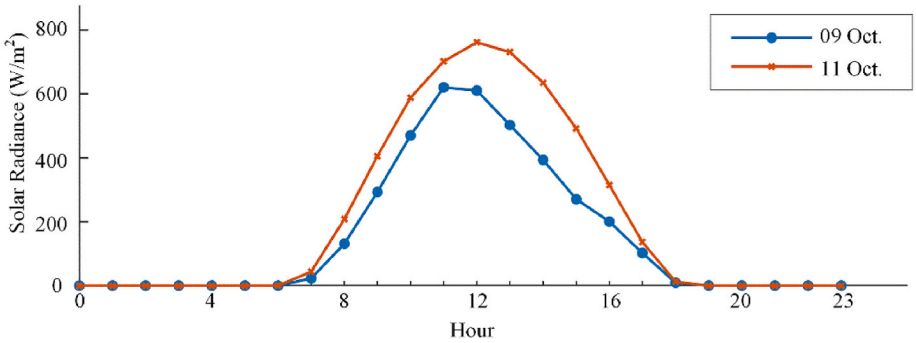

Fig. A.3. Hourly surface solar radiation downwards from the ERA5-Land reanalysis dataset and calculated the domain-averaged instantaneous irradiance over the study region (118–122°E, 31–33.5°N) for both 9 October and 11 October.

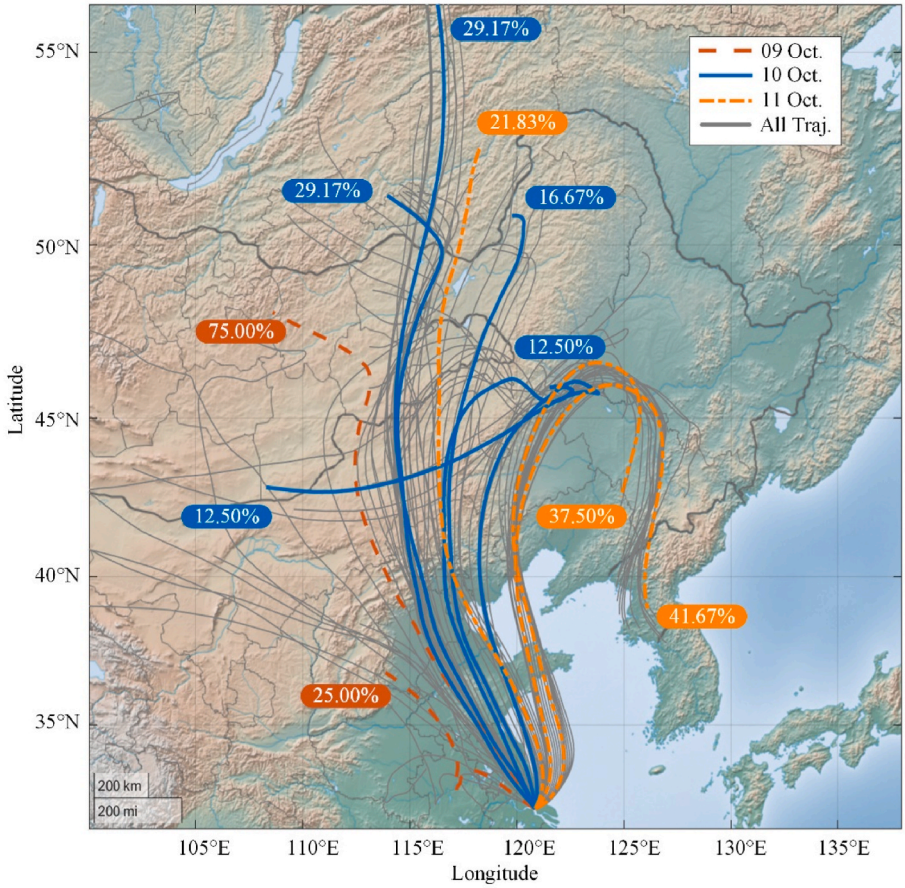

Fig. A.4. 72-h backward trajectories and cluster analysis at Nantong site during 9–11 October (Light gray lines represent raw trajectories; colored lines represent daily cluster trajectories).

Data availability

Measurement data from the cruise campaign used in this study are available from the corresponding author upon request (zhenzhang@nuist.edu.cn).

References

An, J., Duan, Q., Wang, H., Miao, Q., Shao, P., Wang, J., Zou, J., 2015. Fine particulate pollution in the nanjing northern suburb during summer: composition and sources. Environ. Monit. Assess. 187, 561. https://doi.org/10.1007/s10661-015-4765-2.

Atkinson, R., Arey, J., 2003. Gas-phase tropospheric chemistry of biogenic volatile organic compounds: a review. atmospheric environment, The 1997 Southern california ozone study (SCOS97-NARSTO). Dedicat. Mem. Dr. Glen Cass (1947-2001) 37, 197–219. https://doi.org/10.1016/S1352-2310(03)00391-1.

Baars, H., Ansmann, A., Ohneiser, K., Haarig, M., Engelmann, R., Althausen, D., Hanssen, I., Gausa, M., Pietruczuk, A., Szkop, A., Stachlewska, I.S., Wang, D., Reichardt, J., Skupin, A., Mattis, I., Trickl, T., Vogelmann, H., Navas-Guzmán, F., Haefele, A., Acheson, K., Ruth, A.A., Tatarov, B., Müller, D., Hu, Q., Podvin, T., Goloub, P., Veselovskii, I., Pietras, C., Haeffelin, M., Fréville, P., Sicard, M., Comerón, A., Fernández García, A.J., Molero Menéndez, F., Córdoba-Jabonero, C., Guerrero-Rascado, J.L., Alados-Arboledas, L., Bortoli, D., Costa, M.J., Dionisi, D., Liberti, G.L., Wang, X., Sannino, A., Papagiannopoulos, N., Boselli, A., Mona, L., D'Amico, G., Romano, S., Perrone, M.R., Belegante, L., Nicolae, D., Grigorov, I., Gialitaki, A., Amiridis, V., Soupiona, O., Papayannis, A., Mamouri, R.-E., Nisantzi, A., Heese, B., Hofer, J., Schechner, Y.Y., Wandinger, U., Pappalardo, G., 2019. The unprecedented 2017–2018 stratospheric smoke event: decay phase and aerosol properties observed with the EARLINET. Atmos. Chem. Phys. 19, 15183–15198. https://doi.org/10.5194/acp-19-15183-2019.

Burton, S.P., Ferrare, R.A., Hostetler, C.A., Hair, J.W., Rogers, R.R., Obland, M.D., Butler, C.F., Cook, A.L., Harper, D.B., Froyd, K.D., 2012. Aerosol classification using airborne high spectral resolution lidar measurements – methodology and examples. Atmos. Meas. Tech. 5, 73–98. https://doi.org/10.5194/amt-5-73-2012.

Chen, D., Zhao, Q., Li, L., Xia, S., Chen, F., Wei, M., Li, H., Zhang, L., Guan, M., 2022. Shipborne observations of chemical characterization and light extinction of aerosol along the yangtze river, China. Front. Environ. Sci. 10. https://doi.org/10.3389/fenvs.2022.857510.

de Foy, B., Burton, S.P., Ferrare, R.A., Hostetler, C.A., Hair, J.W., Wiedinmyer, C., Molina, L.T., 2011. Aerosol plume transport and transformation in high spectral resolution lidar measurements and WRF-flexpart simulations during the MILAGRO field campaign. Atmos. Chem. Phys. 11, 3543–3563. https://doi.org/10.5194/acp-11-3543-2011.

Derwent, R.G., Jenkin, M.E., Utembe, S.R., Shallcross, D.E., Murrells, T.P., Passant, N.R., 2010. Secondary organic aerosol formation from a large number of reactive man-made organic compounds. Sci. Total Environ. 408, 3374–3381. https://doi.org/10.1016/j.scitotenv.2010.04.013.

Doherty, R.E., 2000. A history of the production and use of carbon tetrachloride, tetrachloroethylene, trichloroethylene and 1,1,1-Trichloroethane in the United States: part 2–Trichloroethylene and 1,1,1-Trichloroethane. Environ. Forensics 1, 83–93. https://doi.org/10.1006/enfo.2000.0011.

Fan, Q., Zhang, Y., Ma, W., Ma, H., Feng, J., Yu, Q., Yang, X., Ng, S.K.W., Fu, Q., Chen, L., 2016. Spatial and seasonal dynamics of ship emissions over the yangtze river delta and east China sea and their potential environmental influence. Environ. Sci. Technol. 50, 1322–1329. https://doi.org/10.1021/acs.est.5b03965.

Fan, S., Liu, C., Xie, Z., Dong, Y., Hu, Q., Fan, G., Chen, Z., Zhang, T., Duan, J., Zhang, P., Liu, J., 2018. Scanning vertical distributions of typical aerosols along the yangtze river using elastic lidar. Sci. Total Environ. 628–629, 631–641. https://doi.org/10.1016/j.scitotenv.2018.02.099.

Gelencsér, A., Siszler, K., Hlavay, J., 1997. Toluene−benzene concentration ratio as a tool for characterizing the distance from vehicular emission sources. Environ. Sci. Technol. 31, 2869–2872. https://doi.org/10.1021/es970004c.

Ghobakhloo, S., Khoshakhlagh, A.H., Morais, S., Mazaheri Tehrani, A., 2023. Exposure to volatile organic compounds in paint production plants: levels and potential human health risks. Toxics 11, 111. https://doi.org/10.3390/toxics11020111.

Hamanaka, R.B., Mutlu, G.M., 2025. Particulate matter air pollution: effects on the respiratory system. J. Clin. Investig. 135, e194312. https://doi.org/10.1172/JCI194312.

Hong, Q., Liu, C., Chan, K.L., Hu, Q., Xie, Z., Liu, H., Si, F., Liu, J., 2018. Ship-based MAX-DOAS measurements of tropospheric NO_2, SO_2, and HCHO distribution along the Yangtze river. Atmos. Chem. Phys. 18, 5931–5951. https://doi.org/10.5194/acp-18-5931-2018.

Huang, K., Zhuang, G., Lin, Y., Fu, J.S., Wang, Q., Liu, T., Zhang, R., Jiang, Y., Deng, C., Fu, Q., Hsu, N.C., Cao, B., 2012. Typical types and formation mechanisms of haze in an eastern Asia megacity. shanghai. Atmos. Chem. Phys. 12, 105–124. https://doi.org/10.5194/acp-12-105-2012.

Huang, Y., Gao, S., Wu, S., Che, X., Yang, Y., Gu, J., Tan, W., Ruan, D., Xiu, G., Fu, Q., 2021. Stationary monitoring and source apportionment of VOCs in a chemical industrial park by combining rapid direct-inlet MSs with a GC-FID/MS. Sci. Total Environ. 795, 148639. https://doi.org/10.1016/j.scitotenv.2021.148639.

Li, Q., Su, G., Li, C., Liu, P., Zhao, X., Zhang, C., Sun, X., Mu, Y., Wu, M., Wang, Q., Sun, B., 2020. An investigation into the role of VOCs in SOA and ozone production in beijing, China. Sci. Total Environ. 720, 137536. https://doi.org/10.1016/j.scitotenv.2020.137536.

Li, Z., Li, C., Ye, X., Fu, H., Wang, L., Yang, X., Wang, X., Zhao, Z., Kan, H., Mellouki, A., Chen, J., 2018. Air quality in the middle and lower reaches of the yangtze river channel: a cruise campaign. Atmos. Chem. Phys. 18, 14445–14464. https://doi.org/10.5194/acp-18-14445-2018.

Li, Z., Ma, Z., Zhang, Z., Zhang, L., Tian, E., Zhang, H., Yang, R., Zhu, D., Li, H., Wang, Z., Zhang, Y., Xu, P., Xu, Y., Wang, D., Wang, G., Kim, M., Yuan, Y., Qiao, X., Li, M., Xie, Y., Guo, S., Liu, K., Jiang, J., 2023. High-density volatile organic compound monitoring network for identifying pollution sources. Sci. Total Environ. 855, 158872. https://doi.org/10.1016/j.scitotenv.2022.158872.

Mai, Z., Wu, R., Gao, W., Li, M., Niu, H., Huang, Z., Liu, M., Tan, G., 2022. Vehicle underway mobile monitoring of volatile organic compounds using online mass spectrometry: application in an industrial park. Environ. Eng. Sci. 39, 718–730. https://doi.org/10.1089/ees.2021.0259.

Ming, L., Jin, L., Li, J., Fu, P., Yang, W., Liu, D., Zhang, G., Wang, Z., Li, X., 2017. PM2.5 in the yangtze river delta, China: chemical compositions, seasonal variations, and regional pollution events. Environ. Pollut. 223, 200–212. https://doi.org/10.1016/j.envpol.2017.01.013.

Panahifar, H., Moradhaseli, R., Khalesifard, H.R., 2020. Monitoring atmospheric particulate matters using vertically resolved measurements of a polarization lidar, in-situ recordings and satellite data over tehran, Iran. Sci. Rep. 10, 20052. https://doi.org/10.1038/s41598-020-76947-w.

Ren, Z., Niu, H., Han, X., Yang, Z., Sun, J., Guo, M., Tan, G., Li, G., 2022. A novel mobile navigation monitoring system based on single photon ionization time-of-flight mass spectrometry: instrumentation development, performance and application. Vacuum 203, 111316. https://doi.org/10.1016/j.vacuum.2022.111316.

Shang, Y., Chen, W., Bao, Q., Yu, Y., Pang, X., Zhang, Y., Guo, L., Fu, J., Feng, W., 2022. Characteristics and source profiles of atmospheric volatile organic compounds (VOCs) in the heavy industrial province of northeast China with cruise monitoring. Front. Environ. Sci. 10. https://doi.org/10.3389/fenvs.2022.1055886.

Shao, Y., 2019. Study on Emission Characteristics and Emission Reduction Potential of Volatile Organic Compounds from Typical Industries (Master). Zhejiang University, China.

Sun, J., Wu, F., Hu, B., Tang, G., Zhang, J., Wang, Y., 2016. VOC characteristics, emissions and contributions to SOA formation during hazy episodes. Atmos. Environ. 141, 560–570. https://doi.org/10.1016/j.atmosenv.2016.06.060.

Tan, W., Liu, C., Wang, S., Xing, C., Su, W., Zhang, C., Xia, C., Liu, H., Cai, Z., Liu, J., 2018. Tropospheric NO_2, SO_2, and HCHO over the east China sea, using ship-based MAX-DOAS observations and comparison with OMI and OMPS satellite data. Atmos. Chem. Phys. 18, 15387–15402. https://doi.org/10.5194/acp-18-15387-2018.

Ting, Y., Liu, D., Morgan, W.T., Allan, J.D., Coe, H., Li, C., Wang, X., Ye, X., Chen, J., 2021. Characterizing black carbon and gaseous pollutants on the yangtze river across eastern China continent. J. Geophys. Res. Atmos. 126. https://doi.org/10.1029/2020JD033488 e2020JD033488.

Wang, D., Szczepanik, D., Stachlewska, I.S., 2019. Interrelations between surface, boundary layer, and columnar aerosol properties derived in summer and early autumn over a continental urban site in warsaw, Poland. Atmos. Chem. Phys. 19, 13097–13128. https://doi.org/10.5194/acp-19-13097-2019.

Wang, H.L., Qiao, L.P., Lou, S.R., Zhou, M., Chen, J.M., Wang, Q., Tao, S.K., Chen, C.H., Huang, H.Y., Li, L., Huang, C., 2015. PM2.5 pollution episode and its contributors from 2011 to 2013 in urban shanghai, China. Atmos. Environ., PM2.5 Research in the Yangtze river Delta: observations. Proc. Model. Health Effect. 123, 298–305. https://doi.org/10.1016/j.atmosenv.2015.08.018.

Wang, J., Zhang, Y., Feng, Y., Zheng, X., Jiao, L., Hong, S., Shen, J., Zhu, T., Ding, J., Zhang, Q., 2016. Characterization and source apportionment of aerosol light extinction with a coupled model of CMB-IMPROVE in Hangzhou, Yangtze River Delta of China. Atmos. Res. 178–179, 570–579. https://doi.org/10.1016/j.atmosres.2016.05.009.

Wang, W., Yu, J., Cui, Y., He, J., Xue, P., Cao, W., Ying, H., Gao, W., Yan, Y., Hu, B., Xin, J., Wang, L., Liu, Z., Sun, Y., Ji, D., Wang, Y., 2018. Characteristics of fine particulate matter and its sources in an industrialized coastal city, ningbo, yangtze river delta, China. Atmos. Res. 203, 105–117. https://doi.org/10.1016/j.atmosres.2017.11.033.

Wang, X., Cai, Y., Wang, J., Zhao, Y., 2021. Concentration monitoring of volatile organic compounds and ozone in xi'an based on PTR-TOF-MS and differential absorption lidar. Atmos. Environ. 245, 118045. https://doi.org/10.1016/j.atmosenv.2020.118045.

Wang, X., Hayeck, N., Brüggemann, M., Abis, L., Riva, M., Lu, Y., Wang, B., Chen, J., George, C., Wang, L., 2020. Chemical characteristics and brown carbon chromophores of atmospheric organic aerosols over the yangtze river channel: a cruise campaign. J. Geophys. Res. Atmos. 125. https://doi.org/10.1029/2020JD032497 e2020JD032497.

Weng, J., Shi, K., Gan, X., Li, G., Huang, Z., 2020. Ship emission estimation with high spatial-temporal resolution in the yangtze river estuary using AIS data. J. Clean. Prod. 248, 119297. https://doi.org/10.1016/j.jclepro.2019.119297.

Wu, Z., Zhang, Y., He, J., Chen, H., Huang, X., Wang, Y., Yu, X., Yang, W., Zhang, R., Zhu, M., Li, S., Fang, H., Zhang, Z., Wang, X., 2020. Dramatic increase in reactive volatile organic compound (VOC) emissions from ships at berth after implementing the fuel switch policy in the Pearl river delta emission control area. Atmos. Chem. Phys. 20, 1887–1900. https://doi.org/10.5194/acp-20-1887-2020.

Xiao, Q., Li, M., Liu, H., Fu, M., Deng, F., Lv, Z., Man, H., Jin, X., Liu, S., He, K., 2018. Characteristics of marine shipping emissions at berth: profiles for particulate matter and volatile organic compounds. Atmos. Chem. Phys. 18, 9527–9545. https://doi.org/10.5194/acp-18-9527-2018.

Yuan, B., Hu, W.W., Shao, M., Wang, M., Chen, W.T., Lu, S.H., Zeng, L.M., Hu, M., 2013. VOC emissions, evolutions and contributions to SOA formation at a receptor site in eastern China. Atmos. Chem. Phys. 13, 8815–8832. https://doi.org/10.5194/acp-13-8815-2013.

Zhang, F., Xiao, B., Liu, Z., Zhang, Y., Tian, C., Li, R., Wu, C., Lei, Y., Zhang, S., Wan, X., Chen, Yubao, Han, Y., Cui, M., Huang, C., Wang, H., Chen, Yingjun, Wang, G., 2024. Real-world emission characteristics of VOCs from typical cargo ships and their potential contributions to secondary organic aerosol and O_3 under low-sulfur fuel policies. Atmos. Chem. Phys. 24, 8999–9017. https://doi.org/10.5194/acp-24-8999-2024.

Zhao, Q., Chen, F., Li, H., Chen, D., Zhang, Y., 2021. Research on air pollution characteristics of the Yangtze river in Jiangsu section. Environ. Sci. Technol.(China) 34, 50–54. https://doi.org/10.19824/j.cnki.cn32-1786/x.2021.0041.

Zhou, T., Huang, J., Huang, Z., Liu, J., Wang, W., Lin, L., 2013. The depolarization–attenuated backscatter relationship for dust plumes. Opt. Express 21, 15195. https://doi.org/10.1364/oe.21.015195.

Zhu, H., Wang, H., Jing, S., Wang, Y., Cheng, T., Tao, S., Lou, S., Qiao, L., Li, L., Chen, J., 2018. Characteristics and sources of atmospheric volatile organic compounds (VOCs) along the mid-lower yangtze river in China. Atmos. Environ. 190, 232–240. https://doi.org/10.1016/j.atmosenv.2018.07.026.

Zou, Y., Yan, X.L., Flores, R.M., Zhang, L.Y., Yang, S.P., Fan, L.Y., Deng, T., Deng, X.J., Ye, D.Q., 2023. Source apportionment and ozone formation mechanism of VOCs considering photochemical loss in guangzhou, China. Sci. Total Environ. 903, 166191. https://doi.org/10.1016/j.scitotenv.2023.166191.